1 **Improving thermodynamic profile retrievals from microwave**

2 **radiometers by including Radio Acoustic Sounding System (RASS)**

3 **observations**

6 Irina V. Djalalova[1,2], David D. Turner[3], Laura Bianco[1,2],

7 James M. Wilczak[2], James Duncan[1,2*], Bianca Adler[1,2] and Daniel Gottas[2]

9 [1] Cooperative Institute for Research in Environmental Sciences (CIRES), Boulder, CO, USA

10 [2] National Oceanic and Atmospheric Administration, Physical Sciences Laboratory, Boulder, CO, USA

11 [3] National Oceanic and Atmospheric Administration, Global Systems Laboratory, Boulder, CO USA

12 [*] Now at WindESCo, Burlington, MA

18 Corresponding author address: Irina V. Djalalova (Irina.V.Djalalova@noaa.gov), NOAA/Physical

19 Science Laboratory, 325 Broadway, mail stop: PSD3, Boulder, CO 80305. Tel.: 303-497-6238.

20 Fax: 303-497-6181.

44 **Abstract**

45   Thermodynamic profiles are often retrieved from the multi-wavelength brightness

46 temperature observations made by microwave radiometers (MWRs) using regression methods

47 (linear, quadratic approaches), artificial intelligence (neural networks), or physical-iterative

48 methods. Regression and neural network methods are tuned to mean conditions derived from

49 a climatological dataset of thermodynamic profiles collected nearby. In contrast, physical-

50 iterative retrievals use a radiative transfer model starting from a climatologically reasonable

51 profile of temperature and water vapor, with the model running iteratively until the derived

52 brightness temperatures match those observed by the MWR within a specified uncertainty.

53   In this study, a physical-iterative approach is used to retrieve temperature and humidity

54 profiles from data collected during XPIA (eXperimental Planetary boundary layer Instrument

55 Assessment), a field campaign held from March to May 2015 at NOAA's Boulder Atmospheric

56 Observatory (BAO) facility. During the campaign, several passive and active remote sensing

57 instruments as well as in-situ platforms were deployed and evaluated to determine their

58 suitability for the verification and validation of meteorological processes. Among the deployed

59 remote sensing instruments were a multi-channel MWR, as well as two radio acoustic sounding

60 systems (RASS), associated with 915-MHz and 449-MHz wind profiling radars.

61   In this study the physical-iterative approach is tested with different observational

62 inputs: first using data from surface sensors and the MWR in different configurations, and then

63 including data from the RASS into the retrieval with the MWR data. These temperature

64 retrievals are assessed against co-located radiosonde profiles. Results show that the

65 combination of the MWR and RASS observations in the retrieval allows for a more accurate

66 characterization of low-level temperature inversions, and that these retrieved temperature

67 profiles match the radiosonde observations better than the temperature profiles retrieved from

68 only the MWR in the layer between the surface and 3 km above ground level (AGL). Specifically,

69 in this layer of the atmosphere, both root mean square errors and standard deviations of the

70 difference between radiosonde and retrievals that combine MWR and RASS are improved by

71 mostly 10-20% compared to the configuration that does not include RASS observations.

72 Pearson correlation coefficients are also improved.

73   A comparison of the temperature physical retrievals to the manufacturer-provided neural

74 network retrievals is provided in Appendix A.

75

76

77

78

79

80

81

82

83

84

85

86

87

1. Introduction

Monitoring the state of the atmosphere for process understanding and for model verification and validation requires observations from a variety of instruments, each one having its set of advantages and disadvantages. Using several diverse instruments allows one to monitor different aspects of the atmosphere, while combining them in an optimized synergetic approach can improve the accuracy of the information available on the state of the atmosphere.

During the eXperimental Planetary boundary layer Instrumentation Assessment (XPIA) campaign, a U.S. Department of Energy sponsored experiment held at the Boulder Atmospheric Observatory (BAO) in Spring 2015, several instruments were deployed (Lundquist et al., 2017) with the goal of assessing their capability for measuring atmospheric boundary layer meteorological variables. XPIA investigated novel measurement approaches, and quantified uncertainties associated with these measurement methods. While the main interest of the XPIA campaign was on wind and turbulence, measurements of other important atmospheric variables were also collected, including temperature and humidity. Among the deployed instruments were two identical microwave radiometers (MWRs) and two radio acoustic sounding systems (RASS), as well as radiosondes launches.

MWRs are passive sensors, sensitive to atmospheric temperature, humidity and liquid water path (LWP), that allow for a high temporal observation of the state of the atmosphere, with some advantages and limitations. In order to estimate profiles of temperature and humidity from the observed brightness temperatures (Tb), several methods could be applied such as regressions, neural network retrievals, or physical retrieval methodologies which can

110   include additional information about the atmospheric state in the retrieval process (e.g., Maahn

111   et al. 2020). Microwave radiative transfer models (e.g., Rosenkranz, 1998; Clough et al. 2005)

112   are commonly used to train statistical retrievals, or as forward models used within physical

113   retrieval methods. Advantages of MWRs include their compact design, the relatively high

114   temporal resolution of the measurements (2-3 minutes), the possibility to observe the vertical

115   structure of both temperature and moisture through the lower part of the troposphere during

116   both clear and cloudy conditions, and their capability to operate in a standalone mode.

117   Disadvantages include limited accuracy in the presence of rain, rather coarse vertical

118   resolution, and the necessity to have a site-specific climatology for retrievals. Other

119   disadvantages include the challenges related to performing accurate calibrations (Küchler et al.,

120   2016, and references within), radio frequency interference (RFI), and the low accuracy on the

121   retrieved LWP especially for values of LWP less than 20 g m^{-2} (Turner 2007).

122   RASS, in comparison, are active instruments that emit a longitudinal acoustic wave

123   upward, causing a local compression and rarefaction of the ambient air. These density

124   variations are tracked by the Doppler radar associated with the RASS, and the speed of the

125   propagating sound wave is measured. The speed of sound is related to the virtual temperature

126   (Tv) (North et al., 1973), and therefore, RASS are used to remotely measure vertical profiles of

127   virtual temperature in the boundary layer. Being an active instrument, the RASS is in general

128   more accurate than a passive instrument (Bianco et al., 2017), but they also come with their

129   own disadvantages. The main limitations of RASS for temperature measurements are the low

130   temporal resolution (typically a 5-min averaged RASS profile is measured once or twice per

131   hour), their limited altitude coverage, and the noise "pollution" that impacts local communities.

132   Adachi and Hashiguchi (2019) have shown that RASS could use parametric speakers to take

133   advantage of their high directivity and very low side lobes. Nevertheless, the maximum height

134   reached by the RASS is limited by sound attenuation, which is a function of both radar

135   frequency and atmospheric conditions (May and Wilczak, 1993) such as temperature, humidity,

136   and the advection of the propagating sound wave out of the radar's field-of-view. Therefore,

137   data availability is usually limited to the lowest several kilometers, depending on the frequency

138   of the radar. In addition, wintertime coverage is usually lower than that in summer, due to

139   increased attenuation of the acoustic signal in cooler and drier environments.

140   To get a better picture of the state of the temperature and moisture structure of the

141   atmosphere, it makes sense to try to combine the information obtained by both MWR and

142   RASS. Integration of different instruments has been and still is a topic of ongoing scientific

143   interest (Han and Westwater 1995; Stankov et al. 1996; Bianco et al., 2005; Engelbart et al.,

144   2009; Cimini et al., 2020; Turner and Löhnert, 2021, to name some). In this study, the focus is

145   on the combination of the MWR and RASS observations in the retrievals to improve the

146   accuracy of the temperature profiles in the lowest 3 km compared to physical retrieval

147   approaches that do not include the information from RASS measurements. Some studies have

148   used analyses from numerical weather prediction (NWP) models as an additional constraint in

149   these variational retrievals (e.g., Hewison 2007; Cimini et al. 2006, 2011; Martinet et al. 2020);

150   however, we have elected not to include model data in this study because we wanted to

151   evaluate the impact of the RASS profiles on the retrievals from a purely observational

152   perspective.

153   This paper is organized as follows: Section 2 summarizes the experimental dataset;

154   Section 3 introduces the principles of the physical retrieval approaches used to obtain vertical

155   profiles of the desired variables; Section 4 produces statistical analysis of the comparison

156   between the different retrieval approaches and radiosonde measurement; finally, conclusions

157   are presented in Section 5.

158

159   **2. XPIA dataset**

160   The data used in our analysis were collected during the XPIA experiment, held in Spring

161   2015 (March-May) at NOAA's BAO site, in Erie, Colorado (Lat.: 40.0451 N, Lon.: 105.0057 W, El.:

162   1584 m MSL). XPIA was the last experiment conducted at this facility, as after almost 40 years

163   of operations the BAO 300-m tower was demolished at the end of 2016 (Wolfe and Lataitis,

164   2018). XPIA was designed to assess the capability of different remote sensing instruments for

165   quantifying boundary layer structure, and was a preliminary study as many of these same

166   instruments were later deployed, among other campaigns, for the second Wind Forecast

167   Improvement Project WFIP2 (Shaw et al., 2019; Wilczak et al., 2019) which investigated flows in

168   complex terrain for wind energy applications, where they were for example used to study cold

169   air pools (Adler et al., 2021) and gap flow characteristics (Neiman et al., 2019; Banta et al.,

170   2020). The list of the deployed instruments included active and passive remote-sensing devices,

171   and in-situ instruments mounted on the BAO tower. Data collected during XPIA are publicly

172   available at https://a2e.energy.gov/projects/xpia. A detailed description of the XPIA

173   experiment can be found in Lundquist et al. (2017), while a specific look at the accuracy of the

174   instruments used in this study can be found in Bianco et al. (2017).

175

2.1 MWR measurements

177   Two identical MWRs (Radiometrics MP-3000A) managed by NOAA (MWR-NOAA) and by

178   the University of Colorado (MWR-CU), were deployed next to each other at the visitor center

179   ~600 m south of the BAO tower (see Lundquist et al., 2017 for a detailed map of the study

180   area). Prior to the experiment, both MWRs were thoroughly serviced (sensor cleaning, radome

181   replacement, etc.) and calibrated using an external liquid nitrogen target and an internal

182   ambient target. MWRs are passive devices which record the natural microwave emission in the

183   water vapor and oxygen absorption bands from the atmosphere, providing measurements of

184   the brightness temperatures. Both MWRs have 35-channels spanning a range of frequencies,

185   with 21 channels in the lower (22-30 GHz) K-band frequency band, of which 8 channels were

186   used during XPIA: 22.234, 22.5, 23.034, 23.834, 25, 26.234, 28 and 30 GHz; and 14 channels in

187   the higher (51-59 GHz) V-band frequency band, of which all were used in XPIA: 51.248, 51.76,

188   52.28, 52.804, 53.336, 53.848, 54.4, 54.94, 55.5, 56.02, 56.66, 57.288, 57.964 and 58.8 GHz.

189   Frequencies in the K-band are more sensitive to water vapor and cloud liquid water, while

190   frequencies in the V-band are sensitive to atmospheric temperature due to the absorption of

191   atmospheric oxygen (Cadeddu et al., 2013). V-band frequencies or channels can also be divided

192   in two categories: the opaque channels, 56.66 GHz and higher, that are more informative in the

193   layer of the atmosphere from the surface to ~1 km AGL, and the transparent channels, 51-56

194   GHz, that are more informative above 1 km AGL. Both MWRs observed at the zenith and at 15-

195   and 165-degree elevation angles in the north-south plane (referred to as oblique elevation

196   scans and used as their average hereafter; note zenith views have a 90-degree elevation angle).

197   However, when MWRs are deployed in locations with unobstructed views, oblique scans can be

198   performed down to 5 degrees elevation angles and may provide better temperature profile

199   accuracy in the lowest 0-1 or even 0-2 km AGL layers (Crewell and Löhnert, 2007).

200   In addition, each MWR was provided with a separate surface sensor to measure

201   pressure, temperature, and relative humidity at the installation level that was ~2.5 m AGL.

202   Vertical profiles of temperature (T), water vapor density (WVD), and relative humidity (RH)

203   were retrieved in real-time during XPIA every 2-3 minutes using a neural network (NN)

204   approach provided by the manufacturer of the radiometer (Solheim et al. 1998a, and 1998b;

205   Ware et al., 2003). Although the physical retrieval configurations used in this study do not

206   exactly match the NN retrieval configurations, a comparison of both physical and neural

207   network retrievals to the radiosonde temperature data is presented in Appendix A.

208   Both MWRs nominally operated from 9 March to 7 May 2015, although the MWR-NOAA

209   was unavailable between 5-27 April 2015. For the overlapping dates, temperature profiles

210   retrieved from the two MWRs showed very good agreement with less than 0.5 $^{\circ}$C bias and

211   0.994 correlation (Bianco et al., 2017). For this reason, and because the MWR-CU was available

212   for a longer time period, only the MWR-CU (hereafter simply called MWR) is used.

213

214   **2.2 WPR-RASS measurements**

215   Two NOAA wind profiling radars (WPRs), operating at frequencies of 915-MHz and 449-

216   MHz, were deployed at the visitor center (same location as the MWR) during XPIA. These

217   systems are primarily designed to measure the vertical profile of the horizontal wind vector, but

218   co-located RASS also enable the observation of profiles of virtual temperature in the lower

219   atmosphere, with different resolutions and height coverages depending on the WPR. Thus, the

220   RASS associated with the 915-MHz WPR (hereafter referred to as RASS 915) measured virtual

221   temperature from 120 to 1618 m with a vertical resolution of 62 m, and the 449 MHz RASS

222   (hereafter referred to as RASS 449) sampled the boundary layer from 217 to 2001 m with a

223   vertical resolution of 105 m. The maximum height reached by the RASS is a function of both

224   radar frequency and atmospheric conditions (May and Wilczak, 1993), and is usually lower for

225   RASS 915 data, as will be shown later in the analysis.

226   The RASS data were processed using a radio frequency interference (RFI)-removal

227   algorithm (performed on the RASS spectra), a consensus algorithm (Strauch et al. 1984)

228   performed on the moment data using a 60% consensus threshold, a Weber-Wuertz outlier

229   removal algorithm (Weber et al., 1993) performed on the consensus averages, and a RASS

230   range-correction algorithm (Görsdorf and Lehmann, 2000) using an average relative humidity

231   setting of 50% determined from the available observations.

232

233   **2.3 BAO data**

234   The BAO 300-m tower was built in 1977 to study the planetary boundary layer (Kaimal

235   and Gaynor 1983). During XPIA, measurements were collected at the surface (2 m) and at six

236   higher levels (50, 100, 150, 200, 250 and 300 m AGL). Each tower level was equipped with 2

237   sonic anemometers on orthogonal booms, and one sensor based on a Sensiron SHT75 solid-

238   state sensor to measure temperature and relative humidity with a time resolution of 1 s, and

239   averaged over five minutes. The more accurate temperature and water vapor observations

240   (Horst et al., 2016) at the BAO tower 2 m AGL level are used in the physical retrieval in place of

241   the less accurate MWR surface sensor.

242

243   **2.4 Radiosonde measurements**

244   Between 9 March and 7 May 2015, while the MWR was operational, radiosondes were

245   launched by the National Center for Atmospheric Research (NCAR) assisted by several students

246   from the University of Colorado over three selected periods, one each in March, April, and May.

247   All radiosondes were Vaisala model RS92. There was a total of 59 launches, mostly four times

248   per day, around 1400, 1800, 2200, and 0200 UTC (0800, 1200, 1600 and 2000 local standard

249   time, LST). The first 35 launches, between 9-19 March, were done from the visitor center, while

250   11 launches between 15-22 April, and 13 launches between 1-4 May, were done from the

251   water tank site, ~1000 meters away from the visitor center (see Lundquist et al., 2017 for a

252   detailed map of the study area). The radiosonde measurements included temperature, dew

253   point temperature, and relative humidity to altitudes usually higher than 10 km AGL, with

254   measurements every few seconds. As a first step, for additional verification, the radiosonde

255   data from the 59 launches taken between 9 March and 4 May 2015 were compared to the BAO

256   tower measurements, up to 300 m AGL. These observed data sets match very well, with a

257   correlation coefficient of 0.99 and a standard deviation of ~0.7 $^\circ$C. However, one radiosonde

258   profile showed a large bias (> 5 $^\circ$C) against all seven levels of BAO temperature measurements

259   and all available Tv measurements from the RASS 915 (eight measurements up to 600 m AGL)

260   and from the RASS 449 (nine measurements up to 1100 m AGL), therefore this particular

261   radiosonde profile was excluded from the statistical analysis. Moreover, while accurate RASS

262 data can be collected during rain, MWR data could be potentially deteriorated due to water

263 deposition on the radome. Therefore, six profiles (three for March 13, and one each on May 1,

264 3 and 4) were eliminated from the statistical evaluation. These restrictions lowered the number

265 of total radiosonde launches used in this study to 52.

266

267 **3. Physical retrievals**

268   One way to combine the active and passive instruments would be to use the RASS

269 observations up to their maximum available height, and stitch them with the profiles obtained

270 from a physical-iterative method using MWR data. To do this, the moisture contribution to the

271 RASS virtual temperatures could be removed by using either the relative humidity measured by

272 the MWR or by a climatology of the moisture term. However, merging these different profiles

273 could result in artificial jumps at the connecting heights.

274   Alternatively, a physical retrieval (PR) iterative approach can be used to retrieve vertical

275 profiles of thermodynamic properties from the MWR and RASS observations in a synergistic

276 manner (e.g., Maahn et al 2020; Turner and Löhnert 2021). In this case, an optimal estimation-

277 based physical retrieval is initialized with a climatologically reasonable profile of temperature

278 and water vapor, and is iteratively repeated until the computed brightness temperatures match

279 those observed by the MWR within the uncertainty of the observed brightness temperatures

280 and the RASS virtual temperatures within their uncertainties (Rodgers, 2000; Turner and

281 Löhnert, 2014; Cimini et al. 2018; Maahn et al. 2020).

282

283   **3.1 Iterative retrieval technique**

284   For this study, the PR uses the *TROPoe* retrieval algorithm (formerly *AERIoe*, Turner and

285   Löhnert 2014; Turner and Blumberg 2019; Turner and Löhnert 2021). This algorithm is able to

286   use radiance data from microwave radiometers, infrared spectrometers, and other

287   observations as input. The microwave radiative transfer model, MonoRTM (Clough et al., 2005),

288   serves as the forward model, which is fully functional for the microwave region and was

289   intensively evaluated previously on MWR measurements (Payne et al. 2008; 2011).

290   We start with the state vector $\mathbf{X_a} = [\mathbf{T, Q,} \text{LWP}]^T$, where superscript T denotes transpose,

291   and vectors and matrices are shown in bold. $\mathbf{T}$ (K) and $\mathbf{Q}$ (g kg^{-1}) are temperature and water

292   vapor mixing ratio profiles at 55 vertical levels from the surface up to 17 km, with the distance

293   between the levels increasing geometrically with height. LWP is the liquid water path in (g m^{-2})

294   that measures the integrated content of liquid water in the entire vertical column above the

295   MWR, and is a scalar. For this study, $\mathbf{X_a}$ has dimensions equal to 111 x 1 (two vectors $\mathbf{T}$ and $\mathbf{Q}$

296   with 55 levels each, and LWP). The retrieval framework of Turner and Blumberg (2019) is used,

297   but only using MWR data (no spectral infrared). Here, we demonstrate the extension of the

298   retrieval to include RASS profiles of $\mathbf{Tv}$, and the resulting impact this has on the retrieved

299   temperature profiles and information content.

300   The observation vector $\mathbf{Y}$ includes temperature and water vapor mixing ratio measured

301   at the surface in-situ, and spectral $\mathbf{Tb}$ measured by the MWR. The MonoRTM model $\mathbf{F}$ is used as

302   the forward model from the current state vector $\mathbf{X}$, and is then compared to the observation

303   vector $\mathbf{Y,}$ iterating until the difference between $\mathbf{F(X)}$ and $\mathbf{Y}$ is small within a specified uncertainty

304   (Eq 1).

305

$$X_{n+1} = X_n + (S_a^{-1} + K^T S_\varepsilon^{-1} K)^{-1} K^T S_\varepsilon^{-1} [Y - F(X_n) + K(X_n - X_a)] \quad (1)$$

307   with

308    $X_a = \begin{bmatrix} T \\ Q \\ LWP \end{bmatrix}$ $S_a = \begin{bmatrix} \sigma_{TT}^2 & \sigma_{TQ}^2 & 0 \\ \sigma_{QT}^2 & \sigma_{QQ}^2 & 0 \\ 0 & 0 & \sigma_{LWP}^2 \end{bmatrix}$ $K_{ij} = \partial F_i / \partial X_j$

309   where i and j in the K_{ij} definition mark channel and vertical level, respectively. The superscripts

310   T and -1 in (1) indicate the transpose and inverse matrix, respectively. The observation vector **Y**

311   and the covariance matrix of the observed data, S_ε, depending on the configuration used, are

312   equal to:

313    $Y_1 = \begin{bmatrix} T_{sfc} \\ Q_{sfc} \\ Tb_{zenith} \end{bmatrix}$ $S_{\varepsilon_1} = \begin{bmatrix} \sigma_{Tsfc}^2 & 0 & 0 \\ 0 & \sigma_{Qsfc}^2 & 0 \\ 0 & 0 & \sigma_{Tb_{zenith}}^2 \end{bmatrix}$

314    $Y_2 = \begin{bmatrix} T_{sfc} \\ Q_{sfc} \\ Tb_{zenith+oblique} \end{bmatrix}$ $S_{\varepsilon_2} = \begin{bmatrix} \sigma_{Tsfc}^2 & 0 & 0 \\ 0 & \sigma_{Qsfc}^2 & 0 \\ 0 & 0 & \sigma_{Tb_{zenith+oblique}}^2 \end{bmatrix}$

315    $Y_3 = \begin{bmatrix} T_{sfc} \\ Q_{sfc} \\ Tb_{zenith+oblique} \\ Tv_{RASS915} \end{bmatrix}$ $S_{\varepsilon_3} = \begin{bmatrix} \sigma_{Tsfc}^2 & 0 & 0 & 0 \\ 0 & \sigma_{Qsfc}^2 & 0 & 0 \\ 0 & 0 & \sigma_{Tb_{zenith+oblique}}^2 & 0 \\ 0 & 0 & 0 & \sigma_{Tv_{RASS915}}^2 \end{bmatrix}$

316    $Y_4 = \begin{bmatrix} T_{sfc} \\ Q_{sfc} \\ Tb_{zenith+oblique} \\ Tv_{RASS449} \end{bmatrix}$ $S_{\varepsilon_4} = \begin{bmatrix} \sigma_{Tsfc}^2 & 0 & 0 & 0 \\ 0 & \sigma_{Qsfc}^2 & 0 & 0 \\ 0 & 0 & \sigma_{Tb_{zenith+oblique}}^2 & 0 \\ 0 & 0 & 0 & \sigma_{Tv_{RASS449}}^2 \end{bmatrix}$

317   Note that the 2-m surface-level observations of temperature and water vapor mixing

318   ratio (T_{sfc} and Q_{sfc}, respectively) are included as part of the observation vector **Y**, and thus the

319   uncertainties (0.5 K for temperature and less than 0.4 g kg^{-1} for mixing ratio) in these

320   observations are included in $\mathbf{S_\varepsilon}$.

321   The mean state vector of the climatological estimates, or a "prior" vector $\mathbf{X_a}$, is a key

322   component in the optimal estimation framework and it is the first guess of the state vector **X**,

323    $\mathbf{X_1}$ in Eq. (1). It provides a constraint on the ill-posed inversion problem. The prior is calculated

324   independently for each month of the year from climatological sounding profiles (using 10 years

325   of data) in the Denver area. **T**he covariance matrix, $\mathbf{S_a}$, of the "prior" vector includes not only

326   temperature or water vapor variances but also the covariances between them. Using around

327   3,000 radiosondes launched by the NWS in Denver, each radiosonde profile is interpolated to

328   the vertical levels used in the retrieval, after which the covariance of temperature and

329   temperature, temperature and humidity, and humidity and humidity is computed for different

330   levels. LWP is arbitrarily assigned in $\mathbf{X_a}$, with large values chosen for its uncertainty in $\mathbf{S_a}$, so that

331   it does not impact (constrain) the retrieval. Presently, the assumed uncertainty in LWP in the

332   prior is assigned to 200 g m^{-2} in TROPoe configuration file.

333   Four configurations are chosen for the observational vector **Y** ($\mathbf{Y_1}$, $\mathbf{Y_2}$, $\mathbf{Y_3}$, and $\mathbf{Y_4}$). In each

334   of these, the surface observations are obtained by the 2-m BAO *in-situ* measurements of

335   temperature and humidity. The MWR provides **Tb** measurements from 22 channels from the

336   zenith scan for the zenith only configuration ($\mathbf{Y_1}$), while when using the zenith plus oblique Tb

337   inputs ($\mathbf{Y_2}$, $\mathbf{Y_3}$, and $\mathbf{Y_4}$) the same 22 channels were used from the zenith scans together with only

338   the four opaque channels (56.66, 57.288, 57.964 and 58.8 GHz) from the oblique scans. Using

339   additional measurements from the co-located radar systems with RASS, the observational

340   vector is further expanded with either RASS 915 (Y_3) or RASS 449 (Y_4) virtual temperature

341   observations. The covariance matrix of the observed data, S_ε, depends on the chosen Y_i as seen

342   in the matrix $S_{\varepsilon i}$ (with i = 1:4) descriptions, with increasing dimensions from Y_1 to Y_2 and

343   additional increasing dimensions to Y_3 or Y_4 through the multi-level measurements of the RASS

344   (Turner and Blumberg, 2019). Table 1 summarizes the observational information included in

345   these four different configurations of the PR.

346

	T_{sfc}	Q_{sfc}	Tb_{zenith}	$Tb_{oblique}$	$TV_{RASS915}$	$TV_{RASS449}$
Y_1 = MWRz	X	X	X			
Y_2 = MWRzo	X	X	X	X		
Y_3 = MWRzo915	X	X	X	X	X	
Y_4 = MWRzo449	X	X	X	X		X

347   *Table 1. Four PR configurations corresponding to the four observational Y_i vectors in Eq. (1).*

348

349   The uncertainty in the MWR Tb observations was set to the standard deviation from a

350   detrended time-series analysis for each channel during cloud-free periods. The method to

351   detect those cloud-free periods is described in detail in Section 3.2. The derived uncertainties

352   ranged from 0.3 K to 0.4 K in the 22 to 30 GHz channels, and 0.4 to 0.8 K in the 52 to 60 GHz

353   channels. We assumed that there was no correlated error between the different MWR

354   channels.

355   For the RASS, co-located RASS and radiosonde profiles were compared and the standard

356   deviation of the differences in Tv were determined as a function of the radar's signal-to-noise

357   ratio (SNR). This relationship resulted in uncertainties that ranged from 0.8 K at high SNR values

358   to 1.5 K at low SNR values. Again, we assumed that there was no correlated error between

359   different RASS heights. Following these assumptions, the covariance matrix S_ε is diagonal.

360   The Jacobian matrix, **K**, is computed using finite differences by perturbing the elements

361   of **X** and rerunning the forward model. It has dimensions m x 111, where m is the length of the

362   vector Y_i, therefore its dimension increases correspondingly with the inclusion of more

363   observational data. **K** makes the "connection" between the state vector and the observational

364   data and should be calculated at every iteration.

365

366   **3.2 Bias-correction of MWR observations using radiosondes or climatology**

367   Observational errors propagate through retrieval into the derived profiles (i.e. the bias

368   of the observed data will contribute to a bias in the retrievals). For that, retrieval uncertainties

369   in Eq. (1) from **Y** = **Y₁** or **Y₂** derive only from uncertainties in surface and MWR data, while

370   retrieval uncertainties from **Y** = **Y₃** or **Y₄** come from uncertainties in the surface, MWR, and RASS

371   measurements.

372   The bias of the retrieval depends on both the absolute accuracy of the forward model

373   and on any observational systematic offset, of which the systematic error in the MWR

374   observations could potentially be reduced through application of an MWR Tb bias-correction

375   procedure. In this study, two different approaches were used for the bias-correction: the first is

376   based on a comparison to the radiosondes, while the second uses climatological profiles. The

377   first method could be used for a field campaign where occasional co-located radiosonde

378   launches are taken, while the second would be used for deployments without any supporting

379   radiosonde observations.

380   For both approaches, the first step is to identify clear-sky periods during which the bias

381   can be estimated (to eliminate uncertainties associated with clouds) and subsequently the bias

382   can be removed from the observed MWR Tbs. One method to identify clear-sky times is to use

383   a time-series of Tb observations in the 30 GHz liquid water sensitive channel of the MWR.

384   The standard deviation of the MWR Tb in the 30 GHz channel is calculated over a time

385   frame of one hour centered at the radiosonde launch time. The data from the zenith scan and

386   the averaged oblique scans are reviewed separately. Liquid-cloud free periods were identified

387   by cases where the temporal standard deviation was small (< 0.4 K), and more than 35

388   radiosonde profiles were classified as being launched in clear skies. The usage of the standard

389   deviation from the time-series from the oblique scans, with the same 0.4 K restriction, reduces

390   the number of the clear-sky radiosonde profiles to 18. For those chosen 18 radiosonde profiles,

391   the Tb is calculated from radiosonde temperature profiles through MonoRTM at each of the

392   MWR channels. The mean difference between these calculated radiosonde Tbs and measured

393   MWR Tbs forms the Tb bias with which the MWR Tb data can be corrected. This bias-correction

394   method will be referred to as 'radiosonde BC'.

395   While this radiosonde BC method can be employed for the XPIA dataset, for other

396   campaigns this approach would not be possible if co-located radiosonde observations were not

397   available. For this situation, an alternative method for correcting the MWR Tb biases is

398   presented. There are often spectral features in the observed minus computed brightness

399   temperature residuals that could not be explained by any physically realistic atmospheric

400   profiles, and can only result because of a calibration error in the observations. This alternative

401   bias-correction method is aimed purely to remove this unphysical spectral signature. In this

402   method, to choose clear-sky periods, the 30 GHz channel MWR Tb data are used on a daily

403   basis. The standard deviation of the MWR Tb is calculated as the average of standard deviations

404   in a one-hour sliding window through all data points of a day. Four clear-sky days were

405   identified using a threshold of 0.4 K on the standard deviation: March 10 and 30, and April 13

406   and 29, 2015. The Tb bias is then computed for each of the 22 channels as the averaged

407   difference between the observed Tb from the MWR zenith observations and the forward model

408   calculated Tbs at zenith using the TROPoe-retrieved profiles (Y_1) of those selected clear-sky

409   days. This method identified spectral calibration errors in the MWR observations that could not

410   be explained by physically realistic atmospheric profiles. This bias-correction technique, which

411   accounts for those unphysical spectral calibration features, will be referred to as 'TROPoe BC'.

412   Fig. 1 shows the Tb biases found for all 22 MWR channels from both bias-correction

413   approaches. The biases calculated with the radiosonde BC scheme are shown for all channels

414   used in our analysis: 22 channels of the zenith scan, in red, and four V-band opaque channels of

415   the oblique scans, in blue. The black and green triangles represent the biases calculated using

416   the TROPoe BC approach for zenith and for zenith+oblique scans, respectively. All biases are

417   presented with associated uncertainties (error bars representing the standard deviation over all

418   radiosondes for radiosonde BC, and mean observation Tb vector uncertainties for chosen four

419   clear-sky days for TROPoe BC).
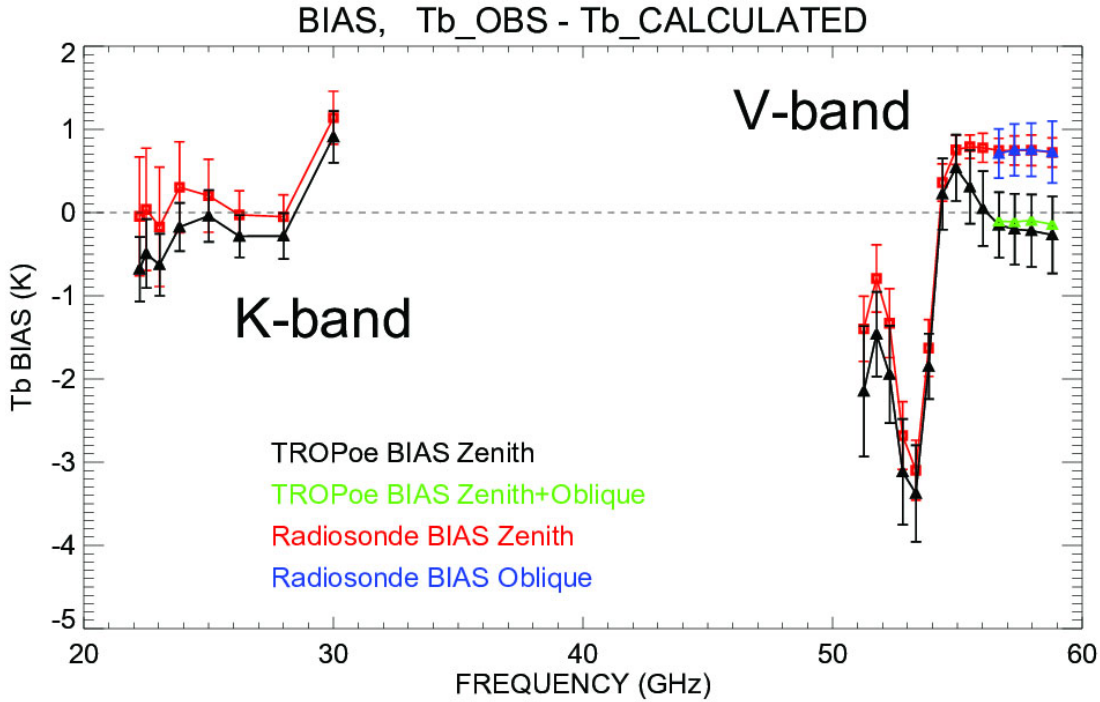
420   *Fig. 1. Tb biases derived from the radiosonde BC method (and TROPoe BC method) in all*

421   *22 MWR channels of the zenith scan in red (and in black), and in the four opaque channels of*

422   *the oblique scans in blue (and in green).*

423

424   The biases from the two bias-correction schemes are within the uncertainties of each

425   other for most of the channels except at the higher frequencies in the V-band. Biases in the

426   most opaque channels are significantly affected by the accuracy of the boundary layer

427   temperature profiles. When TROPoe BC is used, a monthly average prior temperature profile is

428   used in the PR, and thus differences between this prior profile and the actual temperature

429   profile can result in a spectral bias in the more opaque MWR channels. On the contrary, the

430   radiosonde BC uses a direct measurement of the temperature profile (from the radiosonde),

431   and thus is more accurate. It is also important to note that, in both approaches, the biases in

432   the opaque channels for zenith and for oblique scans (for radiosonde BC these are red and blue,

433   respectively; and for the TROPoe BC these are black and green, respectively) are very similar to

434   each other. This supports the assumption that the true bias is nearly independent of the scene,

435   or that the sensitivity to the scene (e.g., zenith or off-zenith) is small.

436   The bias-correction methods were applied by removing the corresponding calculated

437   biases from the MWR Tb observations before the retrievals were performed. Later in Section 4,

438   differences in the retrieved temperature profiles will be shown when using the two bias-

439   correction approaches. These differences will be more evident in the temperature profiles

440   exhibiting near-ground temperature inversions.

441   However, the final goal of this study is not to assess the sensitivity to different bias-

442   correction approaches but to verify that the inclusion of RASS observations does improve

443   retrieved temperature profiles, independently of the bias-correction method used.

444

445   **3.3 Analysis of physical retrieval characteristics**

446   The retrieved profiles of the four different PR configurations presented in Table 1

447   (MWRz, MWRzo, MWRzo915, MWRzo449) were compared to the radiosonde profiles. To

448   compare radiosonde observations against the PR profiles, all radiosonde profiles were

449   interpolated vertically to the same PR heights, and PR profiles were averaged in the time

450   window between 15 minutes before and 15 minutes after each radiosonde launch. Since the

451   radiosonde ascends quite quickly in the lowest kilometers of the atmosphere (~15-20 min to

452   reach 5 km), the 30-minute temporal window is estimated to be representative of the same

453   volume of the atmosphere measured by the radiosonde. BAO tower temperature and mixing

454   ratio data at the seven available levels were used as an additional validation dataset, without

455   any vertical interpolation, averaged in the time window between 15 minutes before and 15

456   minutes after each radiosonde launch.

457   As an example of the different temperature retrievals and their relative performance,

458   data obtained on 17 March 2015 at 2200 UTC are presented in Fig. 2. Temperature profiles up

459   to 2 km AGL retrieved from the four PR configurations (MWRz, MWRzo, MWRzo915,

460   MWRzo449, using the radiosonde BC) are compared to the radiosonde data in red and to the

461   BAO measurements in blue squares. Note that all four of the PRs match the BAO observations

462   reasonably well near the ground. The MWRz and MWRzo profiles are very smooth and depart

463   quite substantially from the radiosonde measurements, being unable to reproduce the more

464   detailed structure of the atmospheric temperature profile measured by the radiosonde, while

465   the MWRzo449 profile (in light-blue) demonstrates a better agreement with both the

466   radiosonde and BAO measurements (blue squares). The MWRzo915 profile (in purple) also tries

467   to follow the elevated temperature inversion observed by the radiosonde, successfully only in

468   the lower part of the atmosphere (below 1 km AGL) where RASS 915 measurements are

469   available. This behavior will be also addressed in the following section and in the statistical

470   analysis presented later in the manuscript.

471
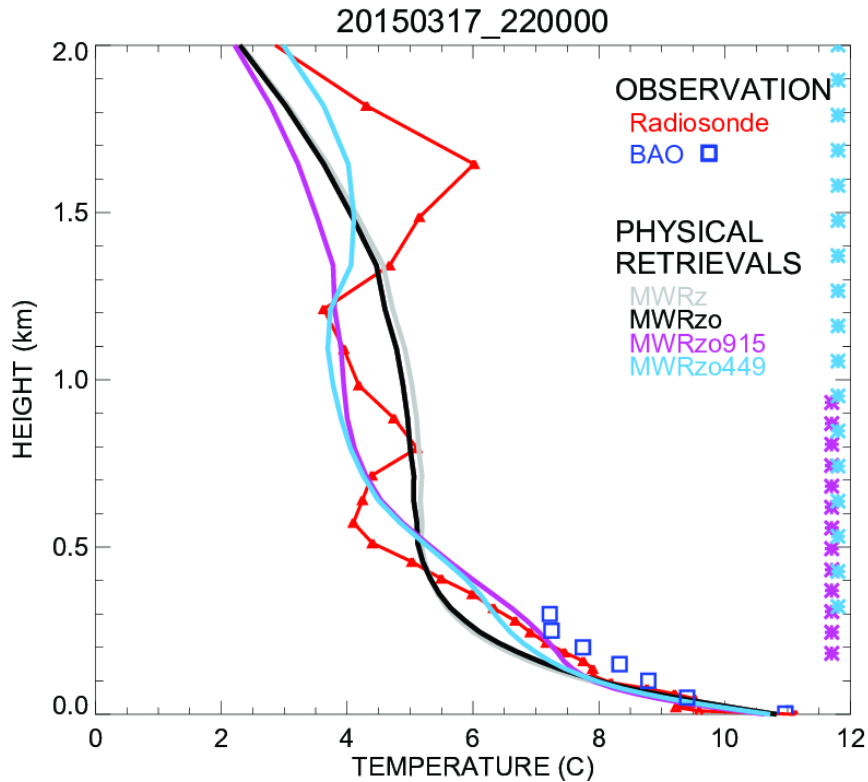
472

473 *Fig. 2. Temperature profiles obtained by the four PR configurations, after applying the*

474 *radiosonde BC on the MWR Tbs: MWRz in gray, MWRzo in black, MWRzo915 in purple, and*

475 *MWRzo449 in light-blue. These retrievals are compared to radiosonde measurements, in red,*

476 *and BAO tower observations, in blue squares. The heights with available RASS virtual*

477 *temperature measurements (RASS 915 in purple and RASS 449 in light-blue) are marked by the*

478 *asterisks on the right Y-axis.*

479

480   An asset of TROPoe is that several characteristics of the PRs can be obtained from two

481 matrices, the averaging kernel, **Akernel,** and the posterior covariance matrix, **Sop** (Masiello et

482 al., 2012; Turner and Löhnert, 2014, Turner and Bloomberg, 2019), calculated as:

483

484          $Akernel = B^{-1}\, K^T\, S_{\varepsilon}^{-1}\, K$ (2)

485   and:

486          $Sop = B^{-1}$ (3)

487   where:

488          $B = S_a^{-1} + K^T\, S_{\varepsilon}^{-1}\, K$

489

490   All matrices, **Akernel**, **Sop**, and **B**, have dimensions 111 x 111 in our configuration. While

491   the top left corner of the **Akernel** matrix (1:55, 1:55) is devoted to temperature, called further

492   in the text **ATkernel**, the next (56:110, 56:110) elements are devoted to the water vapor mixing

493   ratio, called **AQkernel**.

494   The **Akernel** provides useful information about the calculated retrievals, such as vertical

495   resolution and degrees of freedom for signal at each level. The rows of the **Akernel** provide the

496   smoothing functions (Rodgers, 2000) that could be applied to the radiosonde profiles (Eq. 4) to

497   minimize the vertical representativeness error in the comparison between the various retrievals

498   and the radiosonde profiles due to very different vertical resolutions of these profiles (Turner

499   and Löhnert, 2014).

500   Smoothed radiosonde observed profiles can be computed using the averaging kernel,

501   as:

502          $X_{smoothed\_radiosonde} = Akernel\,(X_{radiosonde} - X_a) + X_a$ (4)

503   The **Akernel** in Eq. (2) depends on the retrieval parameters (e.g., which datasets are

504   used in the **Y** vector, the values assumed in the observation covariance matrix S_{ε}, and the

505   sensitivity of the forward model), so for our four PR configurations it is possible to calculate

506   four different kernels from Eq. (2).

507   For each of the four **Akernel**s, a smoothed radiosonde profile can be computed for each

508   radiosonde profile using Eq. (4). In the presence of temperature inversions or other particular

509   structures in the atmosphere, these smoothed profiles can be quite different from each other

510   and also from the original unsmoothed radiosonde profile. Consequently, while comparison of

511   the retrievals to the relative Akernel-smoothed radiosonde profiles can be used to minimize the

512   vertical representativeness effects due to the different vertical resolutions of these profiles, we

513   note that a statistical comparison between the four configurations of the observational vector

514   would not be fair if each of their retrieved profiles is compared to a different Akernel-smoothed

515   radiosonde profile. Therefore, in the statistical analysis presented later in the manuscript

516   (section 4.2), mean bias, root mean square error (RMSE), and Pearson correlation coefficients

517   will be computed between the various TROPoe retrieval configurations and the unsmoothed

518   radiosonde profiles, just interpolated to the same vertical levels of the retrieved profiles.

519   The **ATkernel** can help understand the differences in the retrieved temperature profiles

520   obtained by the configurations using additional RASS data, shown in the example of Fig. 2.

521   Figure 3a includes the temperature profiles of the radiosonde (unsmoothed and **ATkernel**'s

522   smoothed) and PRs of MWRzo and MWRzo449 for the same example as in Fig. 2. Due to the

523   inclusion of RASS measurements, the **ATkernel**-smoothed radiosonde profile of the MWRzo449

524   configuration (dashed light-blue line) is closer to the original radiosonde data (in red) compared

525   to the black dashed profile of the MWRzo's **ATkernel**-smoothed radiosonde profile.

526   Additionally, the rows of the **ATkernel** provide a measure of the retrieval smoothing as a

527   function of altitude, so the full-width half maximum (FWHM) of each **ATkernel** row estimates

528   the vertical resolution of the retrieved solution at each vertical level (Maddy and Barnet, 2008;

529   Merrelli and Turner, 2012). Plots of this vertical resolution as a function of the height for the

530   MWRzo PR and for the MWRzo449 PR are included in Fig. 3b. This plot shows that the

531   additional observations from the RASS 449 significantly improve the vertical resolution of the

532   retrievals.

533   The posterior covariance matrix, **Sop,** provides a measure of the uncertainty of the

534   retrievals while the square root of the diagonal of this matrix is used to specify the 1-σ errors in

535   the profiles of temperature or mixing ratio. Also, **Sop** shows the level-to-level dependency of

536   the retrievals, and in an ideal case should have all non-diagonal elements equal to zero.

537   Converted to a correlation matrix, it is possible to visualize these dependencies, as presented in

538   Fig. 3c, d. The use of additional RASS data (MWRzo449 **Sop**, Fig. 3d) reduces the off-diagonal

539   covariances, therefore substantially decreasing the correlations in those areas compared to the

540   MWRzo **Sop** (Fig. 3c).
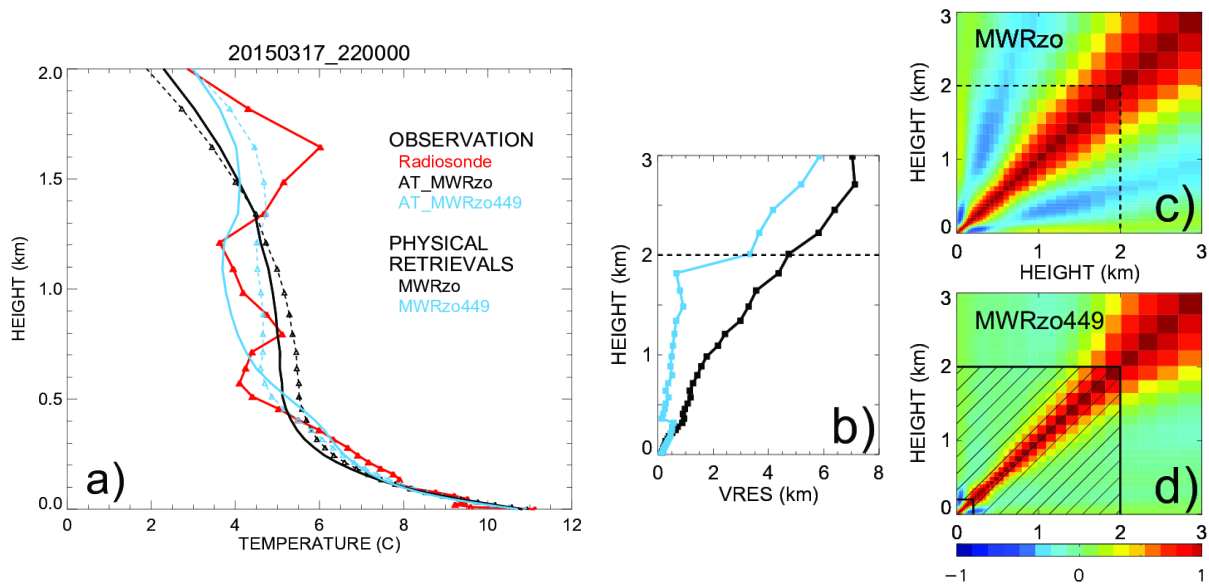
541

*542   Fig. 3. a) observed temperature profiles from radiosonde, in red, from **ATkernel**s smoothed*

*543   radiosonde, **AT_MWRzo** in dashed black, and **AT_MWRzo449** in dashed light-blue; PRs from*

544   MWRzo PR in solid black, and from MWRzo449 PR in solid light-blue. b) vertical resolution

545   (VRES) as a function of the height for the MWRzo PR (black), and for the MWRzo449 PR (light-

*546   blue). c) and d) 3 x 3 km (37 x 37 levels) **Sop** matrices, converted to correlation matrices, for the*

547   MWRzo PR (c), and for the MWRzo449 PR (d). Dashed lines on plots b)-d) mark 2 km AGL.

548   Hatched area on panel d marks the RASS measurement heights.

549

550   To understand the level-to-level correlations among the 4 different retrieval

551   configurations in Table 1, the **Sop** matrices were averaged over all radiosonde events, and

552   converted to correlation matrices (Fig. 4). A clearly visible narrowing of the spread around the

553   main diagonal and correlation reduction in the off-diagonal elements result by adding

554   additional observations, from MWR zenith only (Fig. 4a), to MWR zenith-oblique (Fig. 4b), to

555   the larger impact obtained by the usage of the RASS 915 (Fig. 4c), concluding with the RASS 449

556   (Fig. 4d) data. The mean retrieval uncertainty profile for each of the PR configurations is

557   presented in Fig. 4e. The uncertainty of the MWRzo449 retrieval up to 1 km AGL is around 0.5

558    $^{\circ}$C while the other retrievals have higher uncertainties of up to 1 $^{\circ}$C. The higher accuracy of the

559   MWRzo449 retrievals is because that configuration has more observational information

560   compared to the other retrieval configurations.

561   Other statistically important features to analyze in the PRs, besides their uncertainty,

562   are the vertical resolution already introduced in the example of Fig. 3b, and the degree of

563   freedom for signal (DFS). These two features, derived from the **Akernel**s of each PR

564   configuration, averaged over all radiosonde events, are shown in Fig 4f and 4g. The vertical

565   resolution (Fig. 4f) shows the width of the atmosphere layer used for each retrieval height,

566   computed as the full-width half-maximum value of the averaging kernel. The cumulative DFS

567   profile (Fig. 4g) is a measure of the number of independent pieces of information in the

568   observations below the specified height. For example, at the 1 km AGL level the vertical

569   resolution of MWRzo449 is 0.5 km (i.e. information is from +/- 0.5 km around the retrieval

570   height is considered in the retrieval), while all other retrievals use the information from more

571   than +/- 1.5 km. Also, the DFS, as a cumulative measure, shows an increase in pieces of

572   information from MWRz to MWRzo for the whole profile and from MWRzo to MWRzo915 and

573   to MWRzo449 above ~0.2 km where RASS data are available. The DFS of MWRzo915 is higher

574   compared to the DFS of MWRzo449 in the 0.2-0.5 km AGL layer because RASS 915 data have

575   denser measurements there. It is also important to note that there is no additional information

576   added to any of the retrievals above 2km AGL, i.e. the slope of the cumulative DFS profiles are

577   equal. Despite that, the statistical analysis of the PRs up to 3 km AGL, shown in Section 4, will

578   prove that the retrieval improvements obtained by including the RASS are found even above

579   the height of the RASS measurements availability.

580
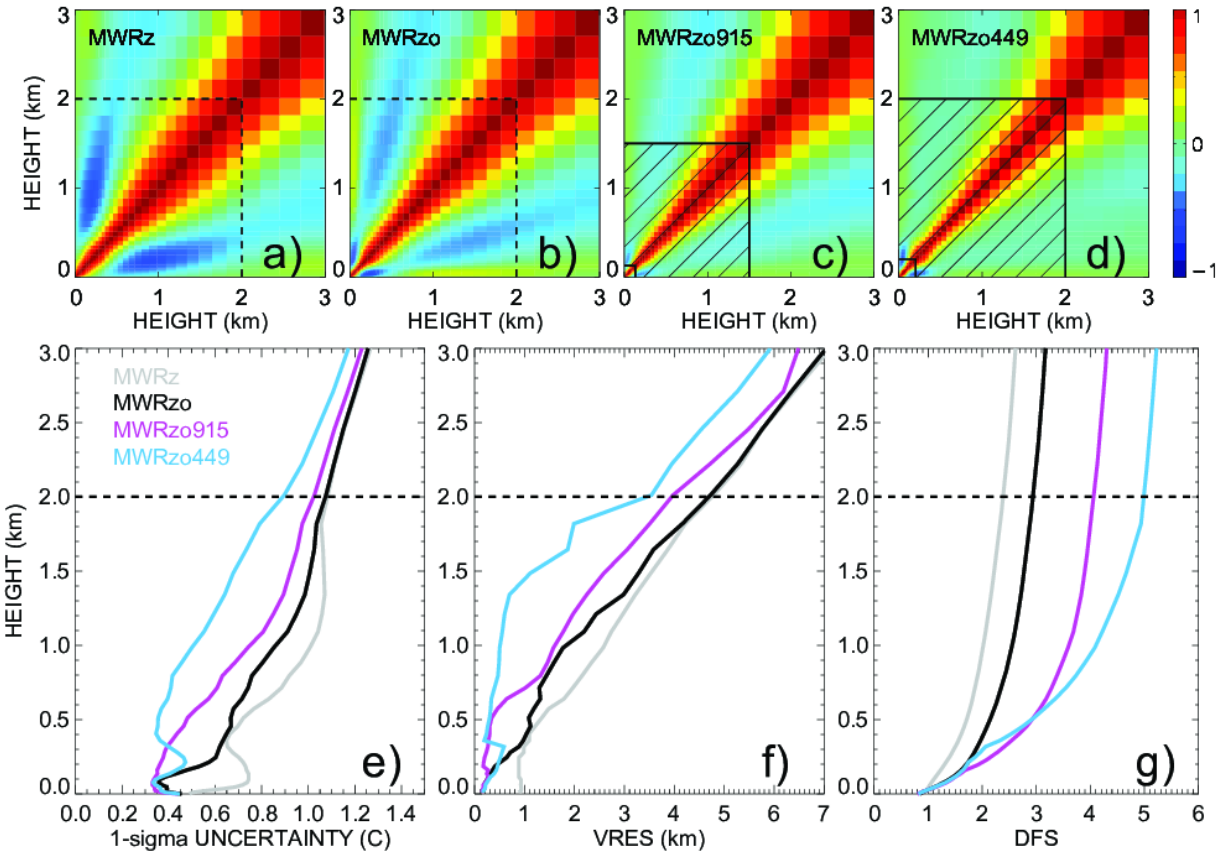
581

582 *Fig. 4. Top row: The mean **Sop**s, displayed as correlation matrices, for (a) MWRz, (b) MWRzo, (c)*

583 *MWRzo915, and (d) MWRzo449, averaged over all radiosonde events. Hatched area on panels*

584 *c) and d) marks the RASS maximum measurement heights. Bottom panels: (e) one-sigma*

585 *uncertainty derived from the posterior covariance matrix in ^oC, (f) vertical resolution (VRES) in*

586 *km, and (g) cumulative Degree of Freedom (DFS) as a function of height for temperature,*

587 *averaged over all radiosonde events (MWRz is in gray, MWRzo is in black, MWRzo915 is in*

588 *purple, and MWRzo449 is in light-blue). Dashed lines mark 2 km AGL on all panels.*

589

590   The improvements from MWRz (in gray) to MWRzo (in black), to MWRzo915 (in purple),

591 and finally to MWRzo449 (in light-blue) are visible in all three panels (Fig 4e-g), whereas

592   MWRzo449 has the lowest 1-σ uncertainty and highest DFS compared to the other PRs,

593   particularly below 2 km AGL, where RASS 449 measurements are available. Finally, it is

594   interesting that below 200 m AGL the MWRzo915 has slightly smaller lowest 1-σ uncertainty

595   and vertical resolution relative to the MWRzo449, as could be expected due to the first

596   available height of the RASS 915 being lower (120 m AGL) than the first available height for the

597   RASS 449 (217 m AGL) and due to the finer vertical resolution of the 915-MHz RASS. This

598   suggests that if additional observations were available in the lowest several 100 m of the

599   atmosphere where RASS measurements are not available, improvements might be even better

600   closer to the surface, where temperature inversions, if present, are sometimes difficult to

601   retrieve correctly.

602

603   **4. Results**

604   **4.1 Statistical analysis of physical retrievals up to 3km AGL**

605   Several cases were found during XPIA when the temperature profile exhibited

606   inversions, with the lowest happening in the surface layer. Figure 5 shows one of the most

607   complex cases, with several temperature inversions visible in the temperature profile from the

608   radiosonde (red line), in the temperature measurements from the BAO tower (blue squares),

609   and in the virtual temperature measured by the RASS 449 (light blue triangles). Note that the

610   virtual temperature profile is in close agreement with the temperature measured by

611   radiosonde.

612
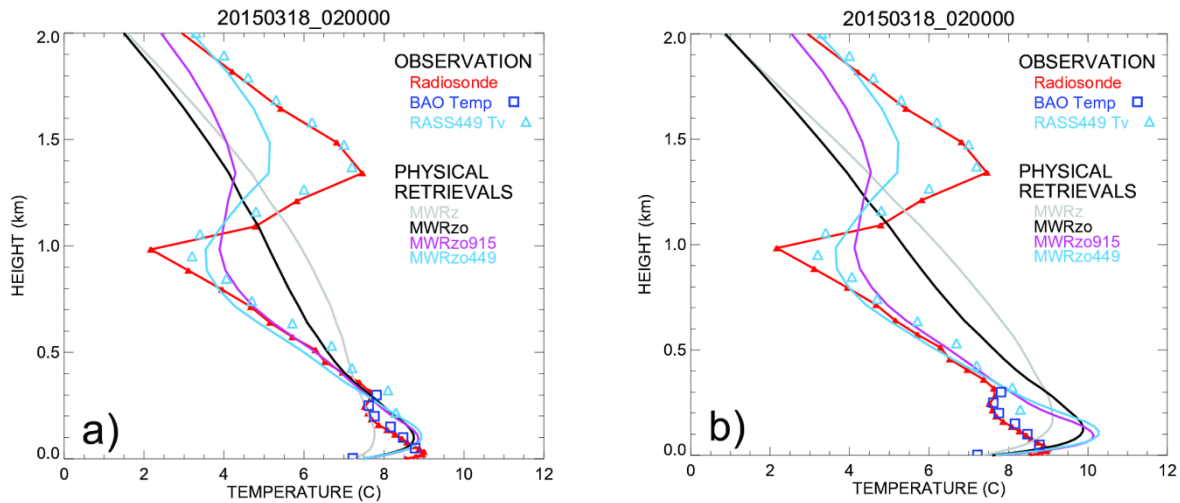
Fig. 5. As in Fig. 2 but for 18 March 2015 at 0200 UTC. The RASS 449 virtual temperature is

included as light blue triangles. a) shows the PRs obtained after applying the radiosonde BC, and

b) shows the PRs obtained after applying the TROPoe BC on the MWR Tbs.

616

Figure 5 also illustrates the difference in the temperature profiles, especially between 0-

300m AGL, for the two different bias-correction schemes, which show noticeable differences in

the biases of the opaque channels (especially important for the near-ground retrievals)

presented in Fig. 1. As expected, the radiosonde BC method yielded a retrieved profile closer to

the radiosonde temperature profile than when using TROPoe BC, for which the inversion in the

temperature profile close to the surface is too accentuated (particularly the black, purple, and

cyan lines, all of which used oblique scan data).

The relative statistical behavior (Pearson correlation, RMSE, and bias) of the PRs for

both temperature and mixing ratio against radiosondes is shown in Figure 6, using both bias-

correction approaches. PRs obtained after applying the radiosonde BC (Fig. 6a) present overall

627   smaller RMSE and bias (the latter almost equal to zero up to 3 km AGL) and slightly higher

628   correlations compared to the statistics of the PRs obtained after applying the TROPoe BC (Fig.

629   6b). This could be expected since for the comparison in Fig. 6a a subset of the radiosondes was

630   already used for the Tb bias correction. Also, the different retrievals show a narrower

631   distribution for the panels in Fig. 6a. Nevertheless, the results obtained when applying either

632   bias-correction methods (in Fig. 6a, b) consistently show the improvement obtained when the

633   RASS observations are used, with relatively smaller bias and RMSE in the 3 km layer AGL. The

634   correlation is mainly improved above 1 km, when RASS observations are included.
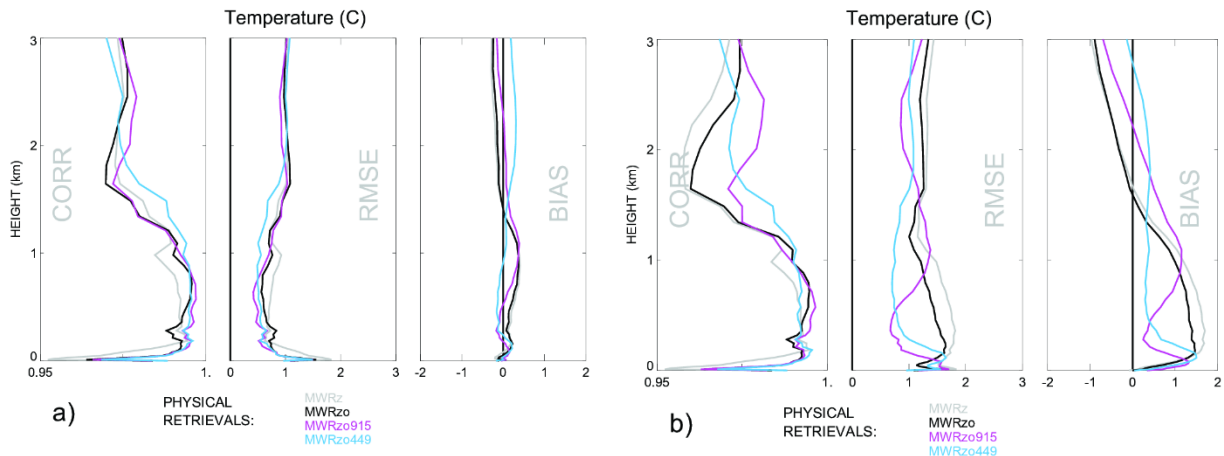
635   *Fig. 6. Pearson correlation, RMSE, and mean bias for temperature profiles of MWRz in gray,*

636   *MWRzo in black, MWRzo915 in purple, and MWRzo449 in light-blue for the radiosonde BC bias-*

637   *correction method in a) and TROPoe BC method in b).*

638

639   Besides temperature profiles, the PRs also provide water vapor mixing ratio profiles. It is

640   understandable that the different configurations of PRs are not noticeably different from each

641   other in relation to moisture, because the Tv observations from the RASS are dominated by the

642   ambient temperature (not moisture), and thus have little impact on the water vapor retrievals.

643   We found that the **AQKernel**s are almost identical for all four PR configurations (not shown).

644   Detailed statistical evaluation of the PRs mixing ratio profiles are presented in Fig, 7, also

645   averaged over all radiosonde events, and show very similar correlations, RMSEs, and biases for

646   all PRs, implying that the impact of including RASS observations in the retrieval is minimal on

647   this variable. Finally, it is noted that Fig. 7 shows the mixing ratio of the data from TROPoe BC.

648   The radiosonde BC mixing ratio results are almost identical.
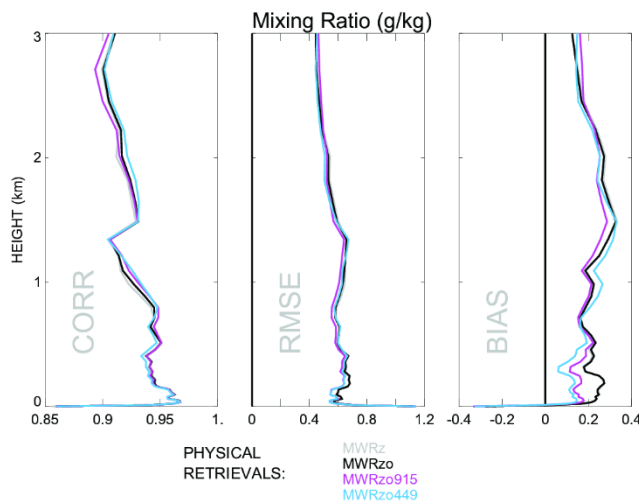
656   *Fig. 7. Same as the panels in Fig. 6b, but for mixing ratio, when using the TROPoe BC method on*

657   *the MWR Tbs.*

658

659   **4.2 Statistics for the profiles least close to the climatology**

660   Physical retrievals use climatological data as a constraint in the retrieval. Statistically,

661   the averaged profiles of both temperature and moisture variables are very close to the

662   climatological averages. However, the most interesting and difficult profiles to retrieve are the

663   cases furthest from climatology (Löhnert and Maier, 2012). To check the behavior of the

664   retrieved data in such "extreme" cases, the RMSE was first calculated for each radiosonde

665   profile relative to the prior profiles for 37 vertical levels from the surface up to 3 km AGL, and

666   then the 15 cases with the largest 0-3 km layer averaged RMSEs compared to the prior were

667   selected.
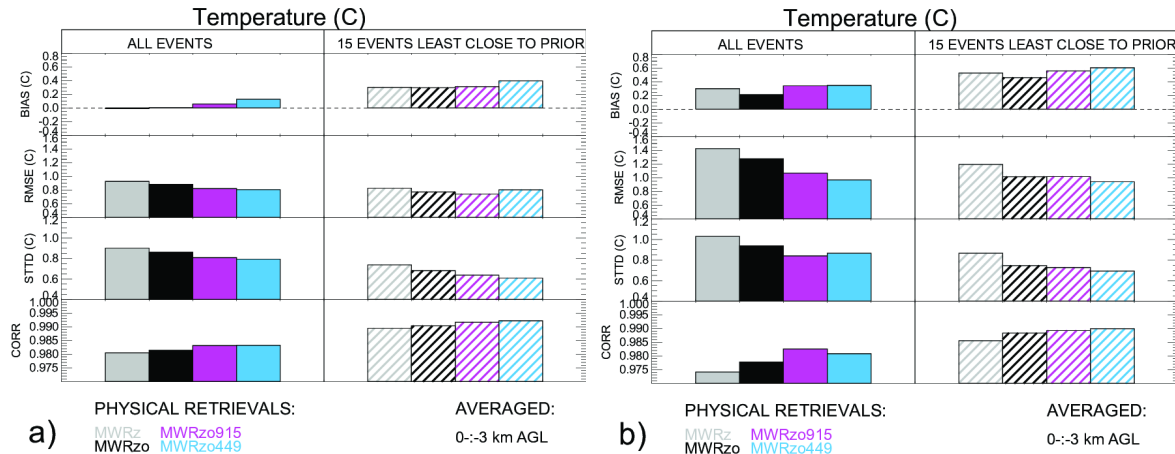
668   *Fig. 8. From top to bottom: biases (retrievals minus radiosonde), RMSEs, standard deviations of*

669   *the difference between retrievals and radiosonde, and Pearson correlations for the four PR*

670   *configurations, averaged from the surface to 3 km AGL, and over all radiosonde data (solid*

671   *boxes), and over the 15 extreme cases (hatched boxes). The data in panels a) use radiosonde BC,*

672   *and in b) TROPoe BC on the MWR Tbs.*

673   Figure 8 shows the temperature statistical analysis for the entire radiosonde data set

674   (solid boxes) and for the fifteen events far from the climatological mean (hatched boxes) for

675   bias, RMSE, standard deviation of the differences between retrievals and radiosonde data, and

676   Pearson correlation, calculated as the weighted averaged over the 37 vertical heights up to 3

677   km AGL[1].

---

[1] The vertical grid used in the PRs is not uniform, with more frequent levels closer to the surface. If a simple average of the data from all levels is used, the near-surface layer will be weighted more compared to the upper levels of the retrievals. To avoid this, a vertical average over the lowest 3 km AGL is performed using weights at each vertical level determined by the distance between the levels.

678    Differences in the statistics when using the entire radiosonde data set or the fifteen

679  extreme profiles are noticeable for all statistical estimators. The PRs that include RASS

680  observations show better performance compared to the strictly MWR-only PR profiles (i.e.,

681  MWRz and MWRzo) for almost all statistical comparisons. This improvement is larger for the

682  PRs using the TROPoe BC (Fig. 8b) compared to the PRs using the radiosonde BC (Fig. 8a). Three

683  statistical estimators, RMSE, standard deviation, and Pearson correlation show overall better

684  values for the 15 extreme cases compared to the whole radiosonde dataset, for all PR

685  configurations and both BC approaches. This is due to the fact that for this dataset the monthly

686  averaged radiosonde profiles (for March and May particularly) depart quite substantially from

687  the monthly prior profiles. For example, the averaged radiosonde profile in March is warmer by

688  ~7 $^{\circ}$C compared to the March prior (and in May by ~5 $^{\circ}$C) in the first 3 km AGL. Consequently,

689  the extreme cases (mostly found in March) have the warmest radiosonde temperature profiles,

690  but are overall closer to the monthly averaged radiosonde profiles.

691    Table 2 includes the same data as in Figure 8 but as a percentage of the improvement,

692  compared to the MWRz retrievals.

693

694

695

696

697

698

0-3 km AGL	ALL EVENTS					15 EVENTS LEAST CLOSE TO THE PRIOR			
	RADIOSONDE BIAS-CORRECTION								
	MWRz	MWRzo	MWRzo RASS915	MWRzo RASS449		MWRz	MWRzo	MWRzo RASS915	MWRzo RASS449
RMSE	0%	5%	11%	13%		0%	7%	10%	3%
STTD	0%	4%	10%	12%		0%	8%	14%	17%
CORR	0%	0.1%	0.3%	0.3%		0%	0.1%	0.2%	0.3%
	TROPoe BIAS-CORRECTION								
RMSE	0%	10%	25%	32%		0%	15%	15%	21%
STTD	0%	9%	18%	16%		0%	14%	16%	20%
CORR	0%	0.4%	0.9%	0.7%		0%	0.3%	0.4%	0.4%

699

700 *Table 2. Retrieval improvements for different RASS/MWR configurations as a percentage*

701 *compared to MWRz.*

702

703   The results presented in Table 2 show improvements in all statistical estimations when

704 including RASS observations, with improvements in RMSE between 10 and 20 %, demonstrating

705 the positive impact derived by the inclusion of the active measurements, regardless of the bias-

706 correction method used, but larger for the TROPoe BC data because there is more room for

707 improvement when this BC method is used. Improvements in the Pearson correlation

708   coefficients are small because correlation, determined during XPIA by the overall temperature

709   structure with height and diurnal cycle, is already good, leaving little room for improvement.

710

711   **4.3 Virtual temperature profile statistics**

712   Using the physical retrieval outputs, "retrieved virtual temperature profiles" can also be

713   calculated. In this section the direct comparison of these retrieved virtual temperature profiles

714   and RASS virtual temperature profiles to the original radiosonde is shown. With this comparison

715   we want to show how the biases of the retrieved profiles relate to the original RASS Tv biases.

716   Figure 9 shows Tv retrieved profile biases compared to the original radiosonde data.

717   These Tv profiles and RASS 915 and RASS 449 Tv bias data are interpolated onto a regular

718   vertical grid, going from 200 m to 1.6 km with a 100 m resolution, for easy comparison.
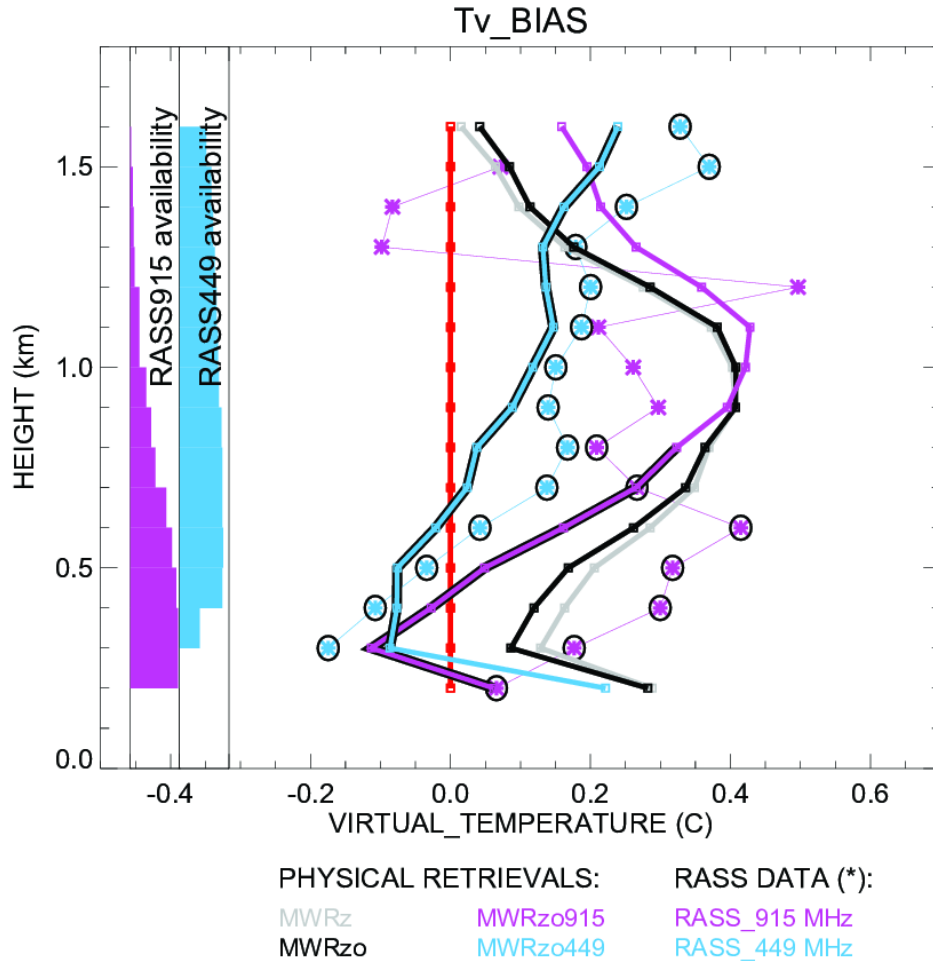
719

720   *Fig. 9. Bias of virtual temperature for all PR configurations compared to the original radiosonde*

721   *measurements. A zero bias is denoted by the red line. RASS data biases are marked by asterisks*

722   *and by additional circles for the RASS data with more than 50% availability, according to the*

723   *availability bar charts on the left.*

724   *All PRs profiles are derived after applying the radiosonde BC method.*

725

726   While RASS 449 data are available at almost all heights up to 1.6 km, the RASS 915 data

727   availability decreases considerably with height, lowering to 50% availability around 800 m AGL.

728   The PRs that include RASS data, MWRzo915 and MWRzo449, are also marked with additional

729   black lines at the heights with at least 50% of relative RASS data availability. In agreement with

730   Fig. 6a, this figure clearly shows the superiority of the MWRzo449 and MWRzo915 (in the layer

731   with > 50% RASS data availability) compared to the MWRz and MWRzo configurations, which

732   do not include RASS data. For MWRzo449, RASS 449 data were almost always available,

733   therefore it is easy to identify a similarity between the Tv bias profiles of the RASS 449 and the

734   PRs including it. Thus, for the MWRzo449 the Tv bias is more uniform through the heights

735   compared to all other PRs that do not include RASS data. Moreover, it is noted a roughly

736   constant offset between the MWRzo449 Tv and RASS 449 Tv biases profiles, with their

737   averaged difference equal to ~0.08 $^{\circ}$C (when the radiosonde BC is used), and to ~0.32 $^{\circ}$C (when

738   the TROPoe BC is used, not shown), over the ~1.3 km (0.3-1.6 km) atmospheric layer where

739   more than 50% of the RASS 449 measurements are available, uniformly distributed through the

740   heights. The inclusion of the RASS into the PRs does reduce the values of the biases in the

741   retrievals even below the values of the RASS biases, because of the combined information from

742   RASS and MWR.

743

744   **5. Conclusions**

745   In this study, data collected during the XPIA field campaign were used to test different

746   configurations of a physical-iterative retrieval (PR) approach in the determination of

747   temperature and humidity profiles from data collected by microwave radiometers, surface

748   sensors, and RASS measurements. The accuracy of several PR configurations was tested: two

749   configurations made use only of surface observations and MWR observed brightness

750   temperature (zenith only, MWRz; and zenith plus oblique, MWRzo); while two others included

751   the active virtual temperature profile observations available from co-located RASS (one, RASS

752   915, associated with a 915-MHz; and the other, RASS 449, associated with a 449-MHz wind

753   profiling radar). Radiosonde launches were used for verification of the retrieved profiles. In

754   Appendix A, the performance of MWRz and MWRzo retrieved profiles and Neural Network

755   retrieved profiles against the radiosondes was evaluated.

756   To remove any observational systematic error in the MWR Tb observations, two bias-

757   correction procedures were tested. The first one takes advantage of the many radiosondes

758   launched during XPIA, and the second one uses climatological profiles. As expected, the

759   radiosonde bias-correction method gives retrieved profiles closer to the radiosonde

760   temperature profiles than when using the climatological based method. Nevertheless, our

761   results show that regardless of the bias-correction method used, the inclusion of the

762   observations from the active RASS instruments in the PR approach improves the accuracy of the

763   temperature profiles by around 10-20% compared to the PR configuration using only surface

764   observations and MWR observed brightness temperature from the zenith scan. Of the PRs

765   configurations tested, generally better statistical agreement is found with the radiosonde

766   observations when the RASS 449 is used together with the surface observations and brightness

767   temperature from the zenith and averaged oblique MWR observations.

768   The **AKernel** and the posterior covariance matrices for temperature are used to derive

769   the one-sigma uncertainty, vertical resolution, and cumulative degree of freedom as a function

770   of height for the different PRs, and the level-to-level correlated uncertainty of the retrievals.

771   Results show that the inclusion of the active instruments improves all of the above-mentioned

772   variables in the 0-3km layer, including at heights between 2-3km that are above the maximum

773   RASS height. Thus, the positive impact of the RASS observations extends into the atmosphere

774   above the height of measurements themselves.

775   Furthermore, 15 cases when temperature profiles from the radiosonde observations

776   were the furthest away from the mean climatological average were selected, and the statistical

777   comparison was reproduced over this subset of cases. These are the cases usually the most

778   difficult to retrieve and the most important to forecast; therefore, it is essential to improve the

779   retrievals in these situations. Even for this subset of selected cases the inclusion of active

780   sensor observations in the PRs is found to be beneficial.

781   Finally, the impact of the inclusion of RASS measurements on the retrieved humidity

782   profiles was considered, but the inclusion of RASS observations did not produce significantly

783   better results, compared to the configurations that do not include them. This was not a surprise

784   as RASS measures virtual temperature, effectively adding very little extra information to the

785   water vapor retrieval. In this case a better option would be to consider adding other active

786   remote sensors such as water vapor differential absorption lidars (DIALs) to the PRs. Turner and

787   Löhnert (2021) showed that including the partial profile of water vapor observed by the DIAL

788   substantially increases the information content in the combined water vapor retrievals.

789   Consequently, to improve both temperature and humidity retrievals a synergy between MWR,

790   RASS, and DIAL systems would likely be necessary.

791

792   **Appendix A**

793   The neural network (NN) retrievals developed by the vendor explicitly for XPIA use a

794 training dataset based on a 5-year climatology of profiles from radiosondes launched at the

795 Denver International Airport, 35 miles south-east from the XPIA site. NN-based MWR vertical

796 retrieval profiles were obtained using the zenith or an average of two oblique elevation scans,

797 15- and 165-degrees (not including the zenith), all with 58 levels extending from the surface up

798 to 10 km, with nominal vertical grid depending on the height (every 50 m from the surface to

799 500 m, every 100 m from 500 m to 2 km, and every 250 m from 2 to 10 km, AGL).

800   Fig. 1A shows composite NN vertical profiles of temperature (separately for the zenith

801 and averaged obliques) calculated for radiosonde launch times, and the corresponding PR

802 profiles already introduced in Fig. 6a, b with additional TROPoe retrievals without any bias-

803 correction. For a proper comparison, only MWRz and MWRzo profiles are used, without

804 including RASS measurements. It has to be noted that since the "NN oblique" retrieval provided

805 by the manufacturer of the radiometer does not include the zenith, this configuration cannot

806 be considered exactly equivalent to the MWRzo PR.
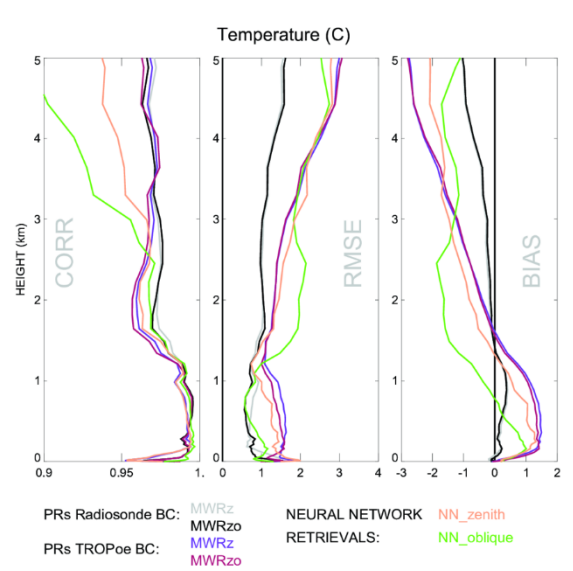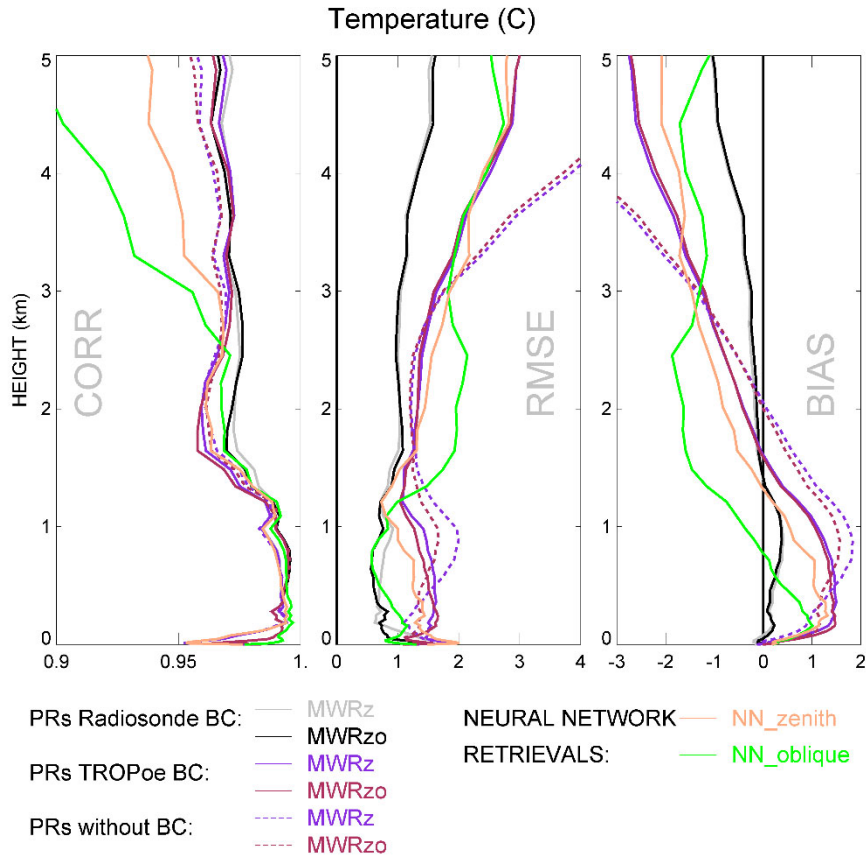
829   *Fig. 1A. Pearson correlation, RMSE, and mean bias for temperature profiles for MWRz in grey*

830   *(and purple) and MWRzo in black (and maroon) when the radiosonde BC (and the TROPoe BC)*

831   *method is applied. TROPoe temperature retrievals without any bias-correction are shown for*

832   *MWRz in dashed purple and for MWRzo in dashed maroon. Included in this figure are the NN*

833   *temperature profiles, from the zenith scan (in beige), and from the averaged oblique scans (in*

834   *green).*

835

836   Another difference to point out is that, while the MWR Tb data have been bias-

837   corrected before being used in the PR configurations, as discussed in Section 3.2, the NN

838   retrievals use the uncorrected Tb, since it was non-trivial to reprocess those retrievals. For

839   additional comparison we included TROPoe retrievals that use uncorrected Tbs. Martinet et al.

840   (2015) showed that when it is possible to bias-correct the MWR Tb before applying the NN

841   retrieval technique, the NN retrievals are not impacted below 1 km AGL, but a clear

842   improvement of NN retrievals in terms of RMSE and bias are observed between 1 and 3 km

843   altitude. As is visible in Fig. 1A, this is the layer of the atmosphere where the NN profiles (beige

844   and green lines) have larger bias and RMSE, compared to the PR profiles.

845   When the radiosonde BC method is used, the MWRz and MWRzo PRs (gray and black

846   lines) present better statistics through the entire profiles shown in Fig. 1A, with larger values of

847   the correlation coefficient, and smaller values of RMSE and bias. The oblique only NN profiles

848   (in green) show comparable statistics to the PRs employing the radiosonde BC method up to 1

849   km AGL, with degraded performances above this height. Above 1 km AGL, the zenith NN

850   profiles (in beige) do better than the oblique NN in terms of RMSE and bias. When the TROPoe

851   BC method is used, the MWRz and MWRzo PRs (purple and maroon lines) perform better than

852   the NN profiles only in terms of RMSE and bias, and only between 1.5 and 3 km AGL. The PRs

853   without any Tb bias-correction (dashed lines in Fig. 1A) clearly indicate that the BC is useful and

854   needed, showing very noticeable degradation in all three statistical measures above 3 km, and

855   larger RMSE and bias in 0.5-1.5 km AGL compared to TROPoe BC method.

856   The better performance obtained by the MWRz and MWRzo PRs that use the

857   radiosonde BC approach demonstrate the importance of having an accurate and reliable

858   method for bias correcting the MWR.

859

860   **Data availability**

861   All data are publicly accessible at the DOE Atmosphere to Electrons Data Archive and

862   Portal, found at https://a2e.energy.gov/projects/xpia (Lundquist et al., 2016).

863

864   **Author contribution**

865   Irina Djalalova completed the primary analysis using the XPIA dataset. Daniel Gottas

866   contributed to the post-processing of the RASS data. Dave Turner modified the TROPoe

867   algorithm to include the RASS data as input. All authors contributed to the analysis of the

868   results. Irina Djalalova prepared the manuscript with contributions from all co-authors.

869

870   **Acknowledgements**

871   We thank all the people involved in XPIA for instrument deployment and maintenance,

872   data collection, and data quality control, and particularly the University of Colorado Boulder for

873   making the CU MWR data available. We are very grateful for the constructive comments and

874   suggestions provided by the two anonymous Referees and by the Editor, which we believe have

875   greatly improved the clarity of the manuscript. Funding for this study was provided by the

876   NOAA/ESRL Atmospheric Science for Renewable Energy (ASRE) program.

877

878 **Competing interests**

879 The authors declare no competing interests.

880

881 **References**

882 Adachi, A. and H. Hashiguchi: Application of parametric speakers to radio acoustic sounding

883   system. **ATMOS MEAS TECH**, **12**, 5699–5715, https://doi.org/10.5194/amt-12-5699-

884   2019, 2019.

885 Adler, B., J. M. Wilczak, L. Bianco, I. Djalalova, J. B. Duncan Jr., D. D. Turner: Observational case

886   study of a persistent cold air pool and gap flow in the Columbia River Basin. **J APPL**

887   **METEOROL CLIM**, 60, 1071-1090, https://doi.org/10.1175/JAMC-D-21-0013.1, 2021.

888 Banta, R. M., and coauthors: Characterizing NWP model errors using Doppler lidar

889   measurements of recurrent regional diurnal flows: Marine-air intrusions into the

890   Columbia River Basin. **MON WEATHER REV**, **148**, 927-953,

891   https://doi.org/10.1175/MWR-D-19-0188.1, 2020.

892 Bianco L., D. Cimini, F. S. Marzano, and R. Ware: Combining microwave radiometer and wind

893   profiler radar measurements for high-resolution atmospheric humidity profiling, **J**

894   **ATMOS OCEAN TECH**, **22**, 949–965, https://doi.org/10.1175/JTECH1771.1, 2005.

895 Bianco, L., K. Friedrich, J. M. Wilczak, D. Hazen, D. Wolfe, R. Delgado, S. Oncley, and J. K.

896   Lundquist: Assessing the accuracy of microwave radiometers and radio acoustic

897   sounding systems for wind energy applications. **ATMOS MEAS TECH**, **10**, 1707-1721,

898   https://doi.org/10.5194/amt-10-1707-2017, 2017.

899   Cadeddu, M. P., J. C. Liljegren, and D. D. Turner: The Atmospheric radiation measurement

900   (ARM) program network of microwave radiometers: instrumentation, data, and

901   retrievals, **ATMOS MEAS TECH**, **6**, 2359–2372, https://doi.org/10.5194/amt-6-2359-

902   2013, 2013.

903   Cimini, D., T. J. Hewison, L. Martin, J. Guldner, C. Gaffard, F. S. Marzano: Temperature and

904   humidity profile retrievals from ground-based microwave radiometers during TUC,

905   **METEOROL Z**, Vol. 15, No. 5, 45-56, DOI: 10.1127/09411-D-2948/2006/0099, 2006.

906   Cimini, D., E. Campos, R. Ware, S. Albers, G. Giuliani, J. Oreamuno, P. Joe, S. E. Koch, S. Cober,

907   and E. Westwater: Thermodynamic Atmospheric Profiling during the 2010 Winter

908   Olympics Using Ground-based Microwave Radiometry, **IEEE T GEOSCI REMOTE**, **49**, 12,

909   https://doi.org/10.1109/TGRS.2011.2154337, 2011.

910   Cimini, D., Rosenkranz, P. W., Tretyakov, M. Y., Koshelev, M. A., and Romano, F.: Uncertainty of

911   atmospheric microwave absorption model: impact on ground-based radiometer

912   simulations and retrievals, **ATMOS CHEM PHYS**, **18**, 15231–15259,

913   https://acp.copernicus.org/articles/18/15231/2018, 2018.

914   Cimini, D., M. Haeffelin, S. Kotthaus, U. Löhnert, P. Martinet, E. O'Connor, C. Walden, M.

915   Collaud Coen, and J. Preissler: Towards the profiling of the atmospheric boundary layer

916   at European scale—introducing the COST Action PROBE. **Bulletin of Atmospheric**

917   **Science and Technology**, **1**, 23–42, https://doi.org/10.1007/s42865-020-00003-8, 2020.

918   Clough, S.A., M. W. Shephard, E. J. Mlawer, J. S. Delamere, M. Iacono, K. E. Cady-Pereira, S.

919   Boukabara and P. D. Brown: Atmospheric radiative transfer modeling: A summary of the

920   AER codes, **J QUANT SPECTROSC RA**, vol 91, no. 2, pp 233-244,

921   https://doi.org/10.1016/j.jqsrt.2004.05.058, 2005.

922   Crewell, S., U. Löhnert: Accuracy of Boundary Layer Temperature Profiles Retrieved With

923   Multifrequency Multiangle Microwave Radiometry, **IEEE T GEOSCI REMOTE**, VOL. 45,

924   NO. 7, JULY 2007, DOI: 10.1109/TGRS.2006.888434, 2007.

925   Engelbart, D., W. Monna, J. Nash: Integrated Ground-Based Remote-Sensing Stations for

926   Atmospheric Profiling, **COST Action 720 Final Report**, EUR 24172,

927   https://doi.org/10.2831/10752, 2009.

928   Görsdorf, U., and V. Lehmann: Enhanced Accuracy of RASS-Measured Temperatures Due to an

929   Improved Range Correction. **J ATMOS OCEAN TECH**, **17 (4)**, 406–416,

930   https://doi.org/10.1175/1520-0426(2000)017<0406:EAORMT>2.0.CO;2, 2000.

931   Han, Y., and E. R. Westwater: Remote sensing of tropospheric water vapor and cloud liquid

932   water by integrated ground-based sensors. **J ATMOS OCEAN TECH**, **12**, 1050-1059, DOI:

933   https://doi.org/10.1175/1520-0426(1995)012<1050:RSOTWV>2.0.CO;2, 1995.

934   Hewison, T.: 1D-VAR Retrieval of Temperature and Humidity Profiles From a Ground-Based

935   Microwave Radiometer, **IEEE T GEOSCI REMOTE**, **45(7)**, 2163–2168,

936   https://doi.org/10.1109/TGRS.2007.898091, 2007.

937   Horst, T. W., S. R. Semmer, and I. Bogoev: Evaluation of Mechanically-Aspirated

938   Temperature/Relative Humidity Radiation Shields, 18th Symposium on Meteorological

939   Observation and Instrumentation, AMS Annual Meeting, New Orleans, LA, 10-15

940   January 2016, https://ams.confex.com/ams/96Annual/webprogram/Paper286839.html,

941   2016.

942   Kaimal, J. C., and J. E. Gaynor: The Boulder Atmospheric Observatory. **J CLIM APPL METEOROL**,

943   **22**, 863–880, https://doi.org/10.1175/1520-0450(1983)022<0863:TBAO>2.0.CO;2, 1983.

944   Küchler, N., D. D. Turner, U. Löhnert,and S. Crewell: Calibrating ground-based microwave

945   radiometers: Uncertainty and drifts, **RADIO SCI**, **51**, 311–327,

946   doi:10.1002/2015RS005826, 2016.

947   Löhnert U. and O. Maier: Operational profiling of temperature using ground-based microwave

948   radiometry at Payerne: prospects and challenges. **ATMOS MEAS TECH**, **5**, 1121–1134,

949   https://doi.org/10.5194/amt-5-1121-2012, 2012.

950   Lundquist, J. K., J. M. Wilczak, R. Ashton, L. Bianco, W. A. Brewer, A. Choukulkar, A. Clifton, M.

951   Debnath, R. Delgado, K. Friedrich, S. Gunter, A. Hamidi, G. V. Iungo, A. Kaushik, B.

952   Kosović, P. Langan, A. Lass, E. Lavin, J. C.-Y. Lee, K. L. McCaffrey, R. K. Newsom, D. C.

953   Noone, S. P. Oncley, P. T. Quelet, S. P. Sandberg, J. L. Schroeder, W. J. Shaw, L. Sparling,

954   C. St. Martin, A. St. Pe, E. Strobach, K. Tay, B. J. Vanderwende, A. Weickmann, D. Wolfe,

955   and R. Worsnop: Assessing state-of-the-art capabilities for probing the atmospheric

956   boundary layer: the XPIA field campaign. **B AM METEOROL SOC**, **98**, 289–314,

957   https://doi.org/10.1175/BAMS-D-15-00151.1, 2017.

958   Maahn, M., D. D. Turner, U. Löhnert, D. J. Posselt, K. Ebell, G. G. Mace, and J. M. Comstock:

959   Optimal estimation retrievals and their uncertainties: What every atmospheric scientist

960   should know. **B AM METEOROL SOC**, **101**, E1512-E1523, https://doi.org/10.1175/BAMS-

961   D-19-0027.1, 2020.

962   Maddy, E. S. and C. D. Barnet: Vertical Resolution Estimates in Version 5 of AIRS Operational

963   Retrievals. **IEEE T GEOSCI REMOTE**, VOL. **46**, NO. 8, AUGUST 2008,

964   https://doi.org/10.1109/TGRS.2008.917498, 2008.

965   Martinet, P., A. Dabas, J.-M. Donier, T. Douffet, O. Garrouste, and R. Guillot: 1D-Var

966   temperature retrievals from microwave radiometer and convective scale model, **TELLUS**

967   **A**, **67:1**, https://doi.org/10.3402/tellusa.v67.27925, 2015.

968   Martinet, P., D. Cimini, F. Burnet, B. Ménétrier, Y. Michel, and V. Unger: Improvement of

969   numerical weather prediction model analysis during fog conditions through the

970   assimilation of ground-based microwave radiometer observations: a 1D-Var study,

971   **ATMOS MEAS TECH**, **13**, 6593–6611, https://doi.org/10.5194/amt-13-6593-2020, 2020.

972   May, P. T. and J. M. Wilczak: Diurnal and Seasonal Variations of Boundary-Layer Structure

973   Observed with a Radar Wind Profiler and RASS. **MON WEATHER REV**, **121**, 673–682,

974   https://doi.org/10.1175/1520-0493(1993)121<0673:DASVOB>2.0.CO;2, 1993.

975   Masiello, G., C. Serio, and P. Antonelli: Inversion for atmospheric thermodynamical parameters

976   of IASI data in the principal components space. **Q J ROY METEOR SOC**, **138**, 103–117,

977   https://doi.org/10.1002/qj.909, 2012.

978   Merrelli, A. M., and D. D. Turner: Comparing information content of upwelling far infrared and

979   midinfrared radiance spectra for clear atmosphere profiling. **J ATMOS OCEAN TECH**, **29**,

980   510–526, https://doi.org/10.1175/JTECH-D-11-00113.1, 2012.

981   Neiman, P. J., D. J. Gottas, and A. B. White: A Two-Cool-Season Wind Profiler–Based Analysis of

982   Westward-Directed Gap Flow through the Columbia River Gorge. **MON WEATHER REV**,

983   **147**, 4653-4680, https://doi.org/10.1175/MWR-D-19-0026.1, 2019.

984   North, E. M., A. M.Peterson, and H. D. Parry: RASS, a remote sensing system for measuring low-

985   level temperature profiles. **B AM METEOROL SOC**, **54**, 912–919, 1973.

986   Payne, V. H., J. S. Delamere, K. E. Cady-Pereira, R. R. Gamache, J.-L. Moncet, E. J. Mlawer, and S.

987   A. Clough: Air-broadened half-widths of the 22- and 183-GHz water-vapor lines. **IEEE T**

988   **GEOSCI REMOTE**, **46**, 3601-3617, https://doi.org/10.1109/TGRS.2008.2002435, 2008.

989   Payne, V. H., E. J. Mlawer, K. E. Cady-Pereira, and J.-L. Moncet: Water vapor continuum

990   absorption in the microwave. **IEEE T GEOSCI REMOTE**, **49**, 2194-2208,

991   https://doi.org/10.1109/TGRS.2010.2091416, 2011.

992   Rodgers, C. D.: Inverse Methods for Atmospheric Sounding: Theory and Practice. Series on

993   Atmospheric, Oceanic and Planetary Physics, Vol. 2, World Scientific, 238 pp, 2000.

994   Rosenkranz, P. W.: Water vapour microwave continuum absorption: A comparison of

995   measurements and models. **RADIO SCI**, **33**, 919–928,

996   https://doi.org/10.1029/98RS01182, 1998.

997   Shaw, W., and Coauthors: The Second Wind Forecast Improvement Project (WFIP 2): General

998   Overview. **B AM METEOROL SOC**, **100(9)**, 1687–1699, https://doi.org/10.1175/BAMS-D-

999   18-0036.1, 2019.

1000   Solheim, F., J. R. Godwin, J., and R. Ware: Passive ground-based remote sensing of atmospheric

1001   temperature, water vapor, and cloud liquid profiles by a frequency synthesized

1002   microwave radiometer. **METEOROL Z**, **7**, 370–376, 1998a.

1003   Solheim F., J. R. Godwin, E. R. Westwater, Y. Han, S. J. Keihm, K. Marsh, R. Ware: Radiometric

1004   profiling of temperature, water vapor and cloud liquid water using various inversion

1005   methods. **RADIO SCI**, **33**, 393–404, https://doi.org/10.1029/97RS03656, 1998b.

1006   Stankov, B. B., E. R. Westwater, and E. E. Gossard: Use of wind profiler estimates of significant

1007   moisture gradients to improve humidity profile retrieval. **J ATMOS OCEAN TECH**, **13**,

1008   1285-1290, DOI:

1009   https://doi.org/10.1175/15200426(1996)013<1285:UOWPEO>2.0.CO;2, 1996.

1010   Strauch, R. G., D. A. Merritt, K. P. Moran, K. B. Earnshaw, and D. V. De Kamp: The Colorado

1011   wind-profiling network. **J ATMOS OCEAN TECH**, **1**, 37–49, https://doi.org/10.1175/1520-

1012   0426(1984)001<0037:tcwpn>2.0.co;2, 1984.

1013   Turner, D. D.: Improved ground-based liquid water path retrievals using a combined infrared

1014   and microwave approach. **J GEOPHYS RES-ATMOS, 112**, D15204,

1015   https://doi.org/10.1029/2007JD008530, 2007.

1016   Turner, D. D., and U. Löhnert: Information content and uncertainties in thermodynamic profiles

1017   and liquid cloud properties retrieved from the ground-based Atmospheric Emitted

1018   Radiance Interferometer (AERI). **J APPL METEOROL CLIM**, **53**, 752–771,

1019   https://doi.org/10.1175/JAMC-D-13-0126.1, 2014.

1020   Turner, D. D., and W. G. Blumberg: Improvements to the AERIoe thermodynamic profile

1021   retrieval algorithm. **IEEE J-STARS**, **12(5)**, 1339–1354,

1022   https://doi.org/10.1109/JSTARS.2018.2874968, 2019.

1023   Turner, D. D., and U. Löhnert: Ground-based Temperature and Humidity Profiling: Combining

1024   Active and Passive Remote Sensors. **ATMOS MEAS TECH**, **14**, 3033–3048,

1025   https://doi.org/10.5194/amt-2020-352, 2021.

1026   Ware R., Solheim F., Carpenter R., and Coauthors: A multi-channel radiometric profiler of

1027   temperature, humidity and cloud liquid. **RADIO SCI**, **38**, No. 4, 8079,

1028   https://doi.org/10.1029/2002RS002856, 2003.

1029   Weber, B. L., D. B. Wuertz, D. C. Welsh, and R. Mcpeek: Quality controls for profiler

1030   measurements of winds and RASS temperatures. **J ATMOS OCEAN TECH**, **10**, 452–464,

1031   https://doi.org/10.1175/1520-0426(1993)010<0452:qcfpmo>2.0.co;2, 1993.

1032   Wilczak, J. M., and Coauthors: The Second Wind Forecast Improvement Project (WFIP2):

1033   Observational Field Campaign. **B AM METEOROL SOC**, **100(9)**, 1701–1723,

1034   https://doi.org/10.1175/BAMS-D-18-0035.1, 2019.

1035   Wolfe, D. E. and R. J. Lataitis: Boulder Atmospheric Observatory: 1977–2016: The end of an era

1036   and lessons learned. **B AM METEOROL SOC**, **99**, 1345–1358,

1037   https://doi.org/10.1175/BAMS-D-17-0054.1, 2018.

1038